

Towards Dynamic Model Identification and Gravity Compensation for the dVRK-Si Patient Side Manipulator

Haoying Zhou^{1,2}, Hao Yang³, Brendan Burkhart², Anton Deguet²,
 Loris Fichera¹, Gregory S. Fischer¹, Jie Ying Wu³ and Peter Kazanzides^{2,4}

Abstract—The da Vinci Research Kit (dVRK) is widely used for research in robot-assisted surgery, but most modeling and control methods target the first-generation dVRK Classic. The recently introduced dVRK-Si, built from da Vinci Si hardware, features a redesigned Patient Side Manipulator (PSM) with substantially larger gravity loading, which can degrade control if unmodeled. This paper presents the first complete kinematic and dynamic modeling framework for the dVRK-Si PSM. We derive a modified DH kinematic model that captures the closed-chain parallelogram mechanism, formulate dynamics via the Euler–Lagrange method, and express inverse dynamics in a linear-in-parameters regressor form. Dynamic parameters are identified from data collected on a periodic excitation trajectory optimized for numerical conditioning and estimated by convex optimization with physical feasibility constraints. Using the identified model, we implement real-time gravity compensation and computed-torque feedforward in the dVRK control stack. Experiments on a physical dVRK-Si show that the gravity compensation reduces steady-state joint errors by 68–84% and decreases end-effector tip drift during static holds from 4.2 mm to 0.7 mm. Computed-torque feedforward further improves transient and position tracking accuracy. For sinusoidal trajectory tracking, computed-torque feedforward reduces position errors by 35% versus gravity-only feedforward and by 40% versus PID-only. The proposed pipeline supports reliable control, high-fidelity simulation, and learning-based automation on the dVRK-Si.

Index Terms—Surgical Robotics, Robot Dynamics, Dynamic Parameter Identification, Gravity Compensation, Model-based Control

I. INTRODUCTION

The da Vinci Research Kit (dVRK, also known as dVRK Classic) [1] has become a widely adopted open-source platform for research in robot-assisted minimally invasive surgery, enabling reproducible studies in teleoperation, perception, learning, and autonomy [2], [3]. Recently, a new dVRK generation built from da Vinci Si hardware (dVRK-Si) [4] has become available to the community. Compared with the first-generation da Vinci components used in the dVRK Classic, the dVRK-Si introduces a redesigned Patient Side Manipulator (PSM) structure that substantially changes the arm’s mass distribution and gravitational loading, as shown in Fig 1. As a result, gravity effects on the dVRK-Si PSM can no longer be treated as negligible, and unmodeled gravity

produces noticeable steady-state errors and drift during static holds, degrading accuracy and responsiveness [5], [6] in both teleoperation and autonomous behaviors.



Fig. 1. Patient Side Manipulator (PSM): dVRK Classic (left), dVRK-Si (right).

Model-based control and realistic simulation both depend on accurate robot dynamics. While dynamic modeling and identification methods have been explored for the dVRK Classic [7]–[10], differences in mechanical components and routing, limit the transferability of previously identified parameters to the dVRK-Si. Moreover, the dVRK-Si platform creates a practical need for gravity compensation that is accurate enough to improve control performance, yet efficient and robust enough to integrate into the real-time control stack.

This paper presents a complete modeling and identification framework for the dVRK-Si PSM and demonstrates its impact on gravity compensation and dynamic position tracking. We first derive a full modified Denavit–Hartenberg (DH) kinematic model for the dVRK-Si PSM, including the closed-chain structure associated with the remote-center-of-motion (RCM) mechanism. We then formulate the robot dynamics using the Euler–Lagrange method and express the inverse dynamics in a linear-in-parameters form. Using an optimized excitation trajectory and a convex optimization-based identification procedure with physical feasibility constraints, we estimate a consistent set of dynamic parameters for a physical dVRK-Si system. With the identified parameters, we compute the gravity vector in real time and implement gravity compensation within the control loop. Furthermore, we compute the full dynamics in real time and add it as a feedforward term within the control loop.

We evaluate the proposed framework on a physical dVRK-Si PSM. Experimental results show that gravity compensation based on the identified model substantially improves static performance, reducing steady-state joint errors by 68–84% and decreasing end-effector tip drift during static holds from 4.2 mm to 0.7 mm. Beyond these headline metrics, we provide a detailed analysis of torque bounds, trajectory-level identification

This work was supported in part by NSF AccelNet award OISE-1927275 and OISE-1927354.

¹Department of Robotics Engineering, Worcester Polytechnic Institute, MA 01609, USA. (Email: hzhou6@wpi.edu)

²Laboratory for Computational Sensing and Robotics, Johns Hopkins University, MD 21218, USA.

³Department of Computer Science, Vanderbilt University, TN 37212, USA.

⁴Department of Computer Science, Johns Hopkins University, MD 21218, USA. (Email: pkaz@jhu.edu)

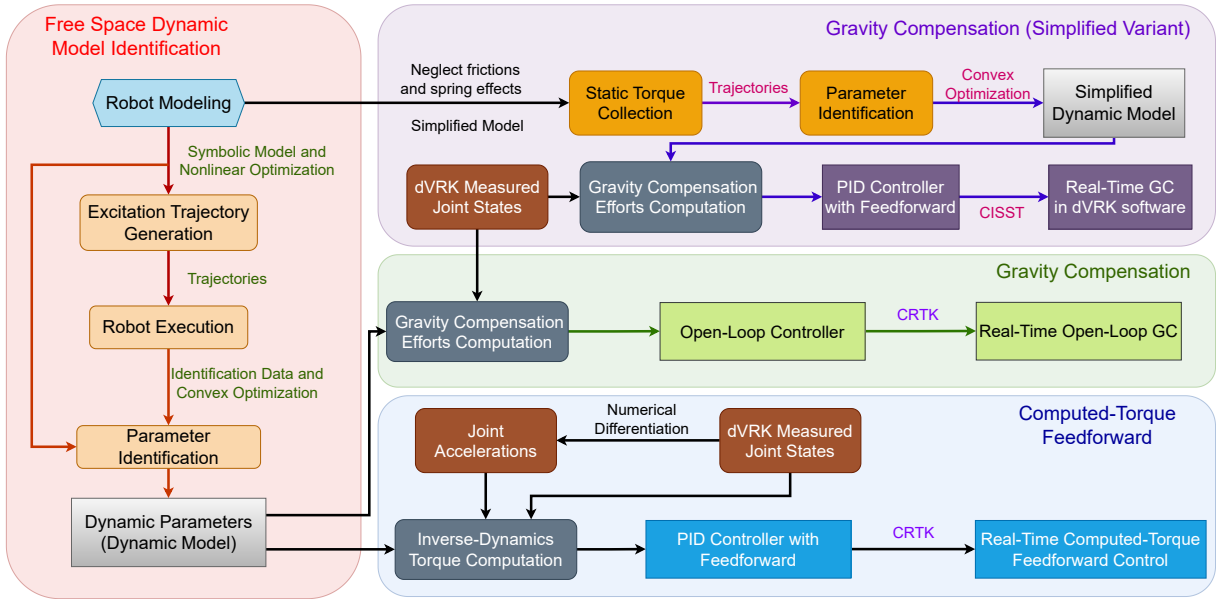


Fig. 2. An overview of the workflow for the proposed dVRK-Si PSM modeling, dynamic parameter identification, and deployment. Free-space dynamic model identification proceeds from symbolic robot modeling to optimized periodic excitation-trajectory generation, hardware execution, and physically consistent parameter estimation via convex optimization to obtain the full dynamic model. The identified model is then deployed through three control implementations: (1) a simplified statics-only gravity-compensation variant fitted from static torque measurements (neglecting friction and spring effects) and integrated into the dVRK software, (2) real-time open-loop gravity compensation implemented, and (3) real-time computed-torque feedforward, where joint accelerations are obtained by numerical differentiation and inverse-dynamics torques are added as a feedforward term to a baseline PID loop.

accuracy, and practical considerations for integrating gravity compensation into the dVRK software stack. For dynamic trajectory tracking, adding the computed-torque feedforward reduces position tracking errors for the first three joints by about 35% compared to gravity feedforward, and by about 40% compared to no feedforward (PID only).

In summary, this work contributes:

- 1) the first complete kinematic and dynamic modeling formulation tailored to the dVRK-Si PSM;
- 2) an excitation-trajectory-driven, physically consistent dynamic model parameter identification pipeline;
- 3) two gravity compensation implementations, including a simplified variant with low computational requirements;
- 4) comprehensive experimental evaluation demonstrating the improved control performance on the dVRK-Si platform;
- 5) an open source implementation at https://github.com/jhu-dvrk/dvrk_psm_dynamics_identification.

II. RELATED WORK

Over the past decade, substantial research efforts have advanced dynamic system identification for the dVRK Classic, with the goals of improving simulation fidelity [11], control performance [12], and force estimation [5], [10], [13]–[16]. Fontanelli et al. [7] identified the dynamic parameters of the Master Tool Manipulator (MTM) and PSM of the dVRK Classic using the method proposed in Sousa et al. [17]. Sang et al. [13] and Piqué et al. [14] estimated the dynamic parameters of the dVRK Classic PSM via Least-square Regression and leveraged the resulting models for sensorless external force estimation for force feedback. Wang et al. [8] developed the first open-source framework for the dVRK Classic MTM and PSM, addressing

the prerequisite for deploying advanced model-based control algorithms, such as those in Lin et al. [12]. More recently, Argin et al. extended this framework by incorporating an improved friction model and employing an Augmented Lagrangian Particle Swarm Algorithm approach [9]. Nevertheless, all aforementioned PSM identification studies focus exclusively on the dVRK Classic and do not address the dVRK-Si platform.

In parallel, rapid progress in artificial intelligence and machine learning has motivated learning-based alternatives for addressing the canonical identification and force estimation problem [18]. Yilmaz et al. proposed a neural-network-based approach for external force estimation [15]. Zhang et al. extended this line of work to estimate both the external wrench and grasping force [19], and Wu et al. further introduced a correction network to compensate for trocar–instrument interactions on an abdominal phantom [16]. Subsequent work has leveraged transfer learning to better accommodate pseudo-clinical settings, enabling force estimation to generalize across different robots, instruments, and ports on an abdominal phantom [20]. Despite their promise, learning-based approaches remain highly sensitive to the quality and coverage of training data; in particular, a mismatch in the training and test workspaces can result in high estimation errors [10]. To mitigate this limitation, Yang et al. [10] proposed a hybrid framework that combines the model-based and learning-based approaches and demonstrated improved force estimation accuracy on the dVRK Classic PSM. Preliminary learning-based investigations on dVRK-Si PSM force estimation and calibration have also been reported [5], [21], although their reliability may be limited by persistent concerns regarding robustness and generalization.

To the best of our knowledge, the only publicly reported

model-based dynamic identification study for the dVRK-Si PSM is our preliminary conference version presented at the Hamlyn Symposium on Medical Robotics [6]. The present manuscript substantially extends [6] with complete derivations, expanded methodology details, and extensive experimental validation.

III. METHODOLOGY

The equations of motion for a robotic manipulator can be expressed using the well-known relation:

$$M(q)\ddot{q} + C(q, \dot{q}) + G(q) = \tau \quad (1)$$

where q represents the joint variables, τ represents the joint torques, $M(q)$ represents the mass matrix of the robot, and $C(q, \dot{q})$, $G(q)$ represent the Coriolis and gravity forces.

Our proposed approach is as follows (Fig. 2):

- (a) Build the kinematic model of the dVRK-Si PSM based on the parameters in Table I;
- (b) Construct the dynamic model of the PSM using the Euler-Lagrangian approach [8];
- (c) Calculate the optimal excitation trajectory based on the given joint constraints and the dynamic model;
- (d) Run the excitation trajectory on the physical dVRK-Si PSM to collect kinematic and dynamic data, and perform preprocessing;
- (e) Solve for the model parameters using a convex optimization approach;
- (f) Evaluate the model at runtime to enable gravity compensation (using only the $G(q)$ term) or computed-torque feedforward (all terms).

Our work builds upon the framework of Wang et al. [8] with an improved Coulomb friction model and excitation trajectory generation approach and delivers a Python 3-compatible, open-source package for dynamic model identification. In addition, we integrate the simplified gravity compensation variant into the dVRK C++ software stack to enable real-time (>1 kHz) execution.

A. Kinematic Model

1) *Joint Coordinates*: To build the relationship between the robot joint motion in the dVRK package [1] and the torque of each motor, multiple types of joint coordinates are defined:

- q^d : the joint coordinates used in the dVRK package on the dVRK-Si PSM. These are related to the motor coordinates q^m via a coupling matrix.
- q^b : the basis joint coordinates which can adequately and independently represent the kinematics of the dVRK-Si PSM. Since the PSM has seven actuated degrees of freedom (DOF), the basis joint coordinates can be represented by $q^b = [q_1 \ q_2 \ \dots \ q_7]^T$.
- q^a : the six auxiliary joint coordinates required to model the RCM or the parallelogram mechanism, which can be represented by a linear combination of q^b (for example, $q_{2''} = -q_2$).
- q : the joint coordinates used in the kinematic modeling of the dVRK-Si PSM in this work (the first 13 parameters in Table I), represented by $q = [(q^b)^T \ (q^a)^T]^T$.

- q^m : the motor coordinates (called *actuator space* in the dVRK software), which are used to model motor inertia and transmission effects.
- q^c : the complete joint coordinates used to attach friction, motor inertia and elastic elements, represented by $q^c = [q^T \ (q^m)^T]^T$.

2) *Joint Coordinate Mapping*: We model the first five joints of the PSM identical to the dVRK software package, which means $q_{1-5} = q_{1-5}^b = q_{1-5}^d$. The dVRK package models the last two joints as follows:

- q_6^d : the angle from the insertion axis to the bisector of the two jaw tips.
- q_7^d : the angle between the two jaw tips.

For convenience, we henceforth use q , rather than q^b , when referring to any of the first seven joints.

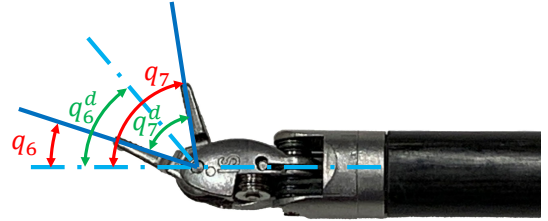


Fig. 3. Modeling of the motion of the PSM gripper.

As shown in Fig. 3, the relationship between q_6 , q_7 and q_6^d , q_7^d can be represented by Eq. 2.

$$\begin{bmatrix} q_6^d & q_7^d \end{bmatrix} = \begin{bmatrix} \frac{q_6 + q_7}{2} & -q_6 + q_7 \end{bmatrix} \quad (2)$$

Meanwhile, since the first four joints are independently driven, the motor coordinates are identical to the joints, which can be represented by $q_{1-4}^d = q_{1-4}^m$. The coupling matrix A_m^d , which maps q_{5-7}^m to q_{5-7}^d , is specific to each instrument and is provided by the dVRK software package [1]; for the Large Needle Driver it is:

$$\begin{bmatrix} q_5^d \\ q_6^d \\ q_7^d \end{bmatrix} = A_m^d \begin{bmatrix} q_5^m \\ q_6^m \\ q_7^m \end{bmatrix} = \begin{bmatrix} 1.0186 & 0 & 0 \\ -0.8306 & 0.6089 & 0.6089 \\ 0 & -1.2177 & 1.2177 \end{bmatrix} \begin{bmatrix} q_5^m \\ q_6^m \\ q_7^m \end{bmatrix} \quad (3)$$

3) *Kinematic Modeling of the dVRK-Si PSM*: Based on our own measurements and manufacturer-provided specifications, we formulate the complete kinematic model of the dVRK-Si PSM, as shown in Fig 4. The detailed kinematic model parameters are summarized in Table I.

B. Dynamic Parameters

For each link k , its dynamic parameter set comprises two components:

- the parameters associated with the link's mass and inertia properties;
- additional parameters capturing internal effects, such as frictions, motor inertia and spring stiffness.

1) *Link Inertial Parameters*: Each rigid link k is characterized by its mass m_k , the position of its center of mass (COM) r_k with respect to link frame k , and its inertia tensor I_{C_k} about the COM. To express the equations of motion in a form that is linear in the dynamic parameters, we adopt the barycentric parameterization [22], where mass m_k , the first moment of mass $h_k \in \mathbb{R}^3 = m_k r_k$ and inertia tensor I_k about frame k

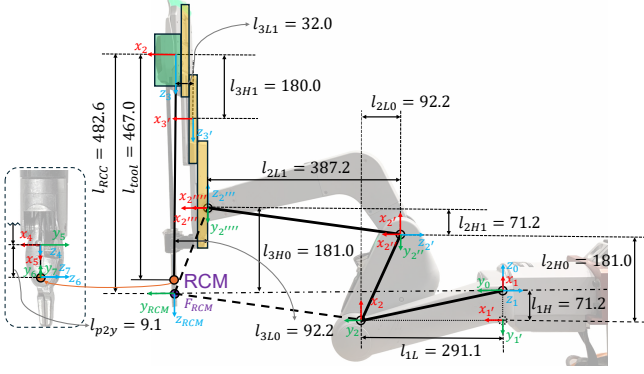


Fig. 4. The planar view of the frame definition for the dVRK-Si PSM. The units of the link lengths are mm. All frames are left-hand frames.

TABLE I
dVRK-Si PSM MODEL DESCRIPTION PARAMETERS

i	Ref	α_{i-1}	α_{i-1}	d_i	θ_i	δ_{Li}	I_{mi}	F_i	K_{si}
1	0	0	$\frac{\pi}{2}$	0	$q_1 + \frac{\pi}{2}$	✓	×	✓	×
1'	1	$-l_{1H}$	$-\frac{\pi}{2}$	0	$\frac{\pi}{2}$	×	×	×	×
2	1'	l_{1L}	0	0	$q_2 - \frac{\pi}{2}$	✓	×	✓	×
2'	2	l_{2L0}	$-\frac{\pi}{2}$	l_{2H0}	0	×	×	×	×
2''	2'	0	$\frac{\pi}{2}$	0	$-q_2 + \frac{\pi}{2}$	✓	×	✓	×
2'''	2''	l_{2L1}	$-\frac{\pi}{2}$	l_{2H1}	0	×	×	×	×
2''''	2'''	0	$\frac{\pi}{2}$	0	q_2	✓	×	✓	×
3	2''''	l_{2L2}	$-\frac{\pi}{2}$	$q_3 + l_{c2}$	0	✓	×	✓	×
3'	3	$-l_{3L}$	0	$l_{3H} - \frac{q_3}{2}$	0	×	×	✓	×
4	3	0	0	l_{tool}	q_4	×	✓	✓	✓
5	4	0	$\frac{\pi}{2}$	0	$q_5 + \frac{\pi}{2}$	×	×	✓	×
6	5	l_{p2y}	$-\frac{\pi}{2}$	0	$q_6 + \frac{\pi}{2}$	×	×	✓	×
7	5	l_{p2y}	$-\frac{\pi}{2}$	0	$q_7 + \frac{\pi}{2}$	×	×	✓	×
* F_{67}	-	0	0	0	$q_7 - q_6$	×	×	✓	×
* M_6	-	0	0	0	q_6^m	×	×	✓	×
* M_7	-	0	0	0	q_7^m	×	×	✓	×

Notes for the table: (1) Ref stands for the reference frame of link i . (2) α_{i-1} , α_{i-1} , d_i and θ_i are the modified DH parameters of link i . (3) δ_{Li} , I_{mi} , F_i and K_{si} are the parameters of link inertia, motor inertia, joint friction, and torsional spring stiffness of link i , respectively. (4) $l_{c2} = l_{3H0} - l_{RCC}$. (5) * denotes that the parameters are not for the kinematic model description. M_6 and M_7 represent the motor model of joint 6 and 7. F_{67} represents the relative motion model between link 6 and 7. q_i^m represents the equivalent motor movements at joint i .

are used to form the dynamic parameter vector. The inertia tensor I_k can be calculated using the parallel axis theorem:

$$I_k = I_{C_k} + m_k \mathbf{S} \begin{pmatrix} \mathbf{h}_k \\ m_k \end{pmatrix}^T \mathbf{S} \begin{pmatrix} \mathbf{h}_k \\ m_k \end{pmatrix} = \begin{bmatrix} I_{kxx} & I_{kxy} & I_{kxz} \\ I_{kxy} & I_{kyy} & I_{kyz} \\ I_{kxz} & I_{kyz} & I_{kzz} \end{bmatrix} \quad (4)$$

where $\mathbf{S}(\cdot)$ denotes the skew-symmetric operator.

The inertial parameters of link k can then be concatenated into a single parameter vector $\theta_{Lk} \in \mathbb{R}^{10}$ as:

$$\theta_{Lk} = [I_{kxx} \quad I_{kxy} \quad I_{kxz} \quad I_{kyy} \quad I_{kyz} \quad I_{kzz} \quad \mathbf{h}_k^T \quad m_k]^T \quad (5)$$

2) *Additional Parameters*: In addition to the inertial parameters of link k , we include the associated joint friction coefficients, motor inertia I_{mk} , and torsional spring stiffness K_{sk} as an additional set of parameters:

$$\theta_{Ak} = [F_{vk} \quad F_{ck} \quad F_{bk} \quad I_{mk} \quad K_{sk}]^T \quad (6)$$

where F_{vk} , F_{ck} denote the viscous and Coulomb friction coefficients, F_{bk} denotes a constant friction bias, and I_{mk} denotes the equivalent motor inertia reflected to joint k through the transmission. Unless otherwise specified, we adopt the indexing convention that link k is actuated by joint k .

Eventually, the parameters associated with all n joints are concatenated to form the full dynamic parameters θ of the dVRK-Si PSM:

$$\theta = [\theta_{L1}^T \quad \theta_{A1}^T \quad \cdots \quad \theta_{Ln}^T \quad \theta_{An}^T]^T \quad (7)$$

where $n = 16$ according to the model description parameters summarized in Table I.

C. Inverse Dynamics Formulation

The inverse dynamic model for the robot with parallelogram mechanism can be calculated using Newton-Euler or Euler-Lagrange methods [23] for the equivalent tree structure and by considering kinematic constraints between joint coordinates [24]. In this work, we select the Euler-Lagrange approach to model the dynamics of the dVRK-Si PSM since it can handle the kinematic constraints more intuitively.

1) *Link Inertia Torque*: The Lagrangian L is calculated as the difference of the kinetic energy K and potential energy P of the robot, $L = K - P$. Friction, motor inertia, and spring stiffness are not included in L and are modeled separately.

The relationship between motor motion \mathbf{q}^m and the torque of each motor i caused by link inertia can be represented by:

$$\tau_{Li}^m(\mathbf{q}^m) = \frac{d}{dt} \frac{\partial L}{\partial \dot{q}_i^m} - \frac{\partial L}{\partial q_i^m} \quad (8)$$

2) *Motor Inertia Torque*: The torques caused by motor inertia can be represented by:

$$\tau_{MI}^m(\ddot{\mathbf{q}}^m) = I_m \ddot{\mathbf{q}}^m \quad (9)$$

where I_m is a diagonal matrix of the motor inertia coefficients of all motors.

3) *Joint Friction Torque*: The torques induced by friction on all joints \mathbf{q}^c can be represented by:

$$\tau_f^c(\dot{\mathbf{q}}^c) = \mathbf{F}_v \dot{\mathbf{q}}^c + \mathbf{F}_c \tanh(\epsilon \dot{\mathbf{q}}^c) + \mathbf{F}_b \quad (10)$$

where \mathbf{F}_v and \mathbf{F}_c are diagonal matrices of the viscous and Coulomb friction coefficients, \mathbf{F}_b denotes the vector of constant friction bias across all joints, and ϵ denotes the diagonal matrix of the joint-velocity-smoothing parameters which can provide a sufficiently wide transition band for near-zero velocities to mitigate sign-switching caused by velocity estimation noise, while remaining close to the signum function at typical operating velocities.

Notably, we utilize the $\tanh(\cdot)$ in place of the discontinuous signum function [25] to obtain a continuous and differentiable approximation of Coulomb friction, thereby improving numerical robustness and reducing sensitivity to velocity noise in the vicinity of $\dot{\mathbf{q}}^c = \mathbf{0}$.

4) *Spring Stiffness Torque*: The torques due to the spring stiffness can be represented by

$$\tau_s^c(\mathbf{q}^c) = \mathbf{K}_s \Delta \mathbf{l}_s \quad (11)$$

where \mathbf{K}_s is a diagonal matrix of the spring stiffness constants of all springs, and $\Delta \mathbf{l}_s$ denotes the equivalent prolongation vector which can be represented by a linear combination of \mathbf{q}^c .

5) *Project non-link torques to motor space:* The joint torques caused by springs and frictions can be projected onto the motor joints, using the Jacobian matrix of their corresponding complete joint coordinates q^c with respect to the motor joint coordinates q^m [24]. Therefore, the overall motor torques τ^m can be represented by

$$\tau^m(q^m, \dot{q}^m, \ddot{q}^m) = \tau_{LI}^m(q^m) + \tau_{MI}^m(\ddot{q}^m) + \frac{\partial q^c}{\partial q^m} [\tau_s^c(q^c) + \tau_f^c(\dot{q}^c)] \quad (12)$$

D. Linear Parameterization

1) *Linear Regressor Formulation:* To identify the dynamic parameters θ in Eq. 7, Eq. 12 can be rewritten linearly in θ [26]:

$$\tau^m(q^m, \dot{q}^m, \ddot{q}^m) = Y(q^m, \dot{q}^m, \ddot{q}^m)\theta \quad (13)$$

where $Y(\cdot)$ is the inverse dynamics regressor matrix, which is also known as the regressor.

2) *Base Parameters Formulation:* Because of the structural dependence (the parallelogram mechanism), the dynamics depends only on certain linear combinations of the parameters, which are the base parameters. It is a minimum set of dynamics parameters which can fully describe the dynamic model of the robot.

To find the base parameters, we introduce a permutation matrix $P \in \mathbb{R}^{p \times p}$, where the regressor $Y \in \mathbb{R}^{n \times p}$ and n denotes the number of joints, as shown in Eq. 7. Then, Eq. 13 can be written as:

$$\begin{aligned} YP &= [Y_b \quad Y_d], \quad P^T\theta = \begin{bmatrix} \theta_b \\ \theta_d \end{bmatrix} \\ \tau^m &= Y\theta = [Y_b \quad Y_d] \begin{bmatrix} \theta_b \\ \theta_d \end{bmatrix} \end{aligned} \quad (14)$$

where $Y_b \in \mathbb{R}^{n \times n_b}$ has n_b linearly independent columns, $Y_d \in \mathbb{R}^{n \times n_d}$ contains the remaining dependent or null column, and $p = n_b + n_d$.

Since Y_d can be written as a linear combination of Y_b , there exists a constant matrix $B_d \in \mathbb{R}^{n_b \times n_d}$ such that

$$Y_d = Y_b B_d \quad (15)$$

Substituting Eq. 15 into Eq. 14, we can obtain:

$$\begin{aligned} \tau^m &= Y_b \beta \\ \beta &= \theta_b + B_d \theta_d \end{aligned} \quad (16)$$

where β denotes the base parameter vector and Y_b is the regressor for the base parameters.

In our work, we utilize the QR decomposition with pivoting [27] to numerically find the base parameters from Eq. 13.

E. Excitation Trajectory Design

1) *Problem Formulation:* To find the periodic excitation trajectories, we utilize a Fourier series to generate data for dynamic model identification [28]. The joint coordinate q_j^m of motor j can be calculated by:

$$q_j^m(t; \mathbf{x}) = q_{oj}^m + \sum_{k=1}^{n_H} \left[\frac{a_{jk}}{k\omega_f} \sin(k\omega_f t) + \frac{b_{jk}}{k\omega_f} \cos(k\omega_f t) \right] \quad (17)$$

where $\omega_f = 2\pi f_f$ is the angular component of the fundamental frequency f_f , n_H is the harmonic number of the Fourier series,

a_{jk} and b_{jk} are the amplitudes of the j^{th} -order sine and cosine function, q_{oj}^m is the position offset, t is time, and \mathbf{x} denotes the coefficients to be optimized, as shown in Eq. 18.

$$\mathbf{x} = [q_{o1}, a_{11}, b_{11}, \dots, a_{1n_H}, \dots, q_{on_s}, \dots, a_{n_s n_H}, b_{n_s n_H}] \quad (18)$$

n_s in Eq. 18 denotes the number of sampling points in one period $T_s = \frac{1}{f_f}$.

Given the joint coordinates $q_j^m(t)$ shown in Eq. 17, we can calculate the motor joint velocity $\dot{q}_j^m(t)$ and acceleration $\ddot{q}_j^m(t)$ using the first and second derivative of $q_j^m(t)$, as shown in Eq. 19.

$$\begin{aligned} \dot{q}_j^m(t; \mathbf{x}) &= \sum_{k=1}^{n_H} [a_{jk} \cos(k\omega_f t) - b_{jk} \sin(k\omega_f t)] \\ \ddot{q}_j^m(t; \mathbf{x}) &= -\sum_{k=1}^{n_H} (k\omega_f) [a_{jk} \sin(k\omega_f t) + b_{jk} \cos(k\omega_f t)] \end{aligned} \quad (19)$$

Substituting the calculated $q_j^m(t)$, $\dot{q}_j^m(t)$ and $\ddot{q}_j^m(t)$ into Eq. 16, we can stack all samples into one data matrix:

$$\begin{bmatrix} \tau^m(t_1) \\ \tau^m(t_2) \\ \vdots \\ \tau^m(t_{n_s}) \end{bmatrix} = \begin{bmatrix} Y_b(t_1) \\ Y_b(t_2) \\ \vdots \\ Y_b(t_{n_s}) \end{bmatrix} \beta = \mathbf{W}_b(\mathbf{x})\beta \quad (20)$$

where $\mathbf{W}_b(\mathbf{x})$ denotes the regression matrix for the excitation trajectory generation problem.

Therefore, the excitation trajectory design problem amounts to choosing \mathbf{x} to yield a well-conditioned $\mathbf{W}_b(\mathbf{x})$, which can improve the numerical stability and accuracy of the parameter identification.

2) *Nonlinear Optimization:* To obtain a well-conditioned $\mathbf{W}_b(\mathbf{x})$, we minimize the L2-norm condition number $\kappa(\cdot)$ of the matrix $\mathbf{W}_b(\mathbf{x})$:

$$\kappa(\mathbf{W}_b) = \frac{\sigma_{max}(\mathbf{W}_b)}{\sigma_{min}(\mathbf{W}_b)} \quad (21)$$

where $\sigma(\cdot)$ denotes the singular value of the matrix.

Then, we scale each column of \mathbf{W}_b by dividing each element by the column's Root Mean Square (RMS), and obtain the RMS-scaled matrix $\tilde{\mathbf{W}}_b$. We utilize the RMS-scaled matrix for optimization to avoid scale domination [29].

The optimization is constrained by the given joint position and velocity limits. Moreover, we optimize the log-condition number $\log(\kappa(\cdot))$ since the logarithm compresses the wide dynamic range of $\kappa(\cdot)$ and improves numerical stability and optimizer convergence by reducing sensitivity when $\kappa(\cdot)$ becomes large [30]. Therefore, the overall optimization problem can be presented as:

$$\begin{aligned} \min_{\mathbf{x}} \quad & J_{traj}(\mathbf{x}) = \log(\kappa(\tilde{\mathbf{W}}_b(\mathbf{x}))) \\ \text{s.t.} \quad & q_{j,min}^m \leq q_j^m(t) \leq q_{j,max}^m, \quad \forall j \\ & \dot{q}_{j,min}^m \leq \dot{q}_j^m(t) \leq \dot{q}_{j,max}^m, \quad \forall j \end{aligned} \quad (22)$$

where j denotes the motor joint j .

In our work, we select the fundamental frequency $f_f = 0.18$ Hz and the harmonic number $n_H = 6$ to generate the excitation trajectory [8]. Eventually, the constrained nonlinear optimization problem is solved using pyOpt [31] with the Sequential Least Squares Quadratic Programming (SLSQP) algorithm [32], yielding the optimal coefficient vector \mathbf{x} .

F. Data Collection and Preprocessing

We collect data by executing the generated excitation trajectory at 200 Hz using the dVRK software framework on a dVRK-Si PSM equipped with a Large Needle Driver, as shown in Fig. 5. Joint positions, velocities and torques are recorded by subscribing to the dVRK-ROS topics. Joint accelerations are then obtained via numerical differentiation of the measured velocities. Finally, the signals are preprocessed using a sixth-order low-pass filter with cutoff frequency of 5.4 Hz, applied in forward and backward directions to achieve zero-phase delay [8].

G. Physical Consistency Constraints

To reduce overfitting, we utilize physical consistency constraints when solving for the dynamic parameters.

1) *Constraints for Dynamic Model Identification for Gravity Compensation:* When solving the dynamic parameters for the gravity compensation problem, we use the physical consistency constraints as follows:

- The mass of each link is positive, $m_k > 0$.
- The COM of each link k , \mathbf{r}_k is inside its convex hull, $\mathbf{h}_k - m_k \mathbf{r}_{lk} \geq 0$ and $m_k \mathbf{r}_{uk} - \mathbf{h}_k \geq 0$, where \mathbf{r}_{lk} and \mathbf{r}_{uk} denotes the lower and upper bounds of \mathbf{r}_k , respectively [17].
- The viscous and Coulomb friction coefficients for each joint k are positive, i.e. $F_{vk} > 0$ and $F_{ck} > 0$.
- The stiffness of spring k is positive, i.e. $K_{sk} > 0$.
- The inertia of motor k is positive, i.e. $I_{mk} > 0$.

2) *Constraints for General Dynamic Model Identification:* When solving the dynamic parameters for the full dynamic system identification problem, we retain all of the aforementioned constraints and further impose one additional constraint as follows:

- The inertia matrix of each link k is positive definite [33], and its eigenvalues should follow the triangle inequality conditions [34].

The constraints regarding the mass and inertia properties of link k can be derived into an equivalent with linear matrix inequalities (LMIs) [17]:

$$\mathbf{D}_k(\boldsymbol{\theta}_{Lk}) = \begin{bmatrix} \frac{1}{2} \text{tr}(\mathbf{I}_k) \mathbf{I}_{3 \times 3} - \mathbf{I}_k & \mathbf{h}_k \\ \mathbf{h}_k^T & m_k \end{bmatrix} > \mathbf{0} \quad (23)$$

where $\mathbf{I}_{3 \times 3} \in \mathbb{R}^{3 \times 3}$ denotes the identity matrix.

We add the experimental lower and upper bounds to m_k , F_{vk} , F_{ck} and K_{sk} into the open-source dynamic model identification framework.

H. Model Parameter Identification

The data is collected along with sampling time defined in Eq. 20, and thus we can obtain the regression matrix \mathbf{W} and dependent variable vector \mathbf{b} :

$$\mathbf{W} = \begin{bmatrix} Y(t_1) \\ Y(t_2) \\ \dots \\ Y(t_{n_s}) \end{bmatrix}, \quad \mathbf{b} = \begin{bmatrix} \tau^m(t_1) \\ \tau^m(t_2) \\ \dots \\ \tau^m(t_{n_s}) \end{bmatrix} \quad (24)$$

Therefore, the identification problem can be formulated into an optimization problem which minimizes the scaled squared residual errors $\mathbf{J}(\boldsymbol{\theta})$ with respect to the decision vector $\boldsymbol{\theta}$:

$$\mathbf{J}(\boldsymbol{\theta}) = \omega_i \|\mathbf{W}\boldsymbol{\theta} - \mathbf{b}\|_2^2 \quad (25)$$

where the scale factor $\omega_i = \frac{1}{\max(\tau_i^m) - \min(\tau_i^m)}$ for each motor i .

We use the CVXPY package [35] with the splitting conic solver (SCS) [36] to solve the convex optimization identification problem, subject to the constraints identified in Section III-G.

I. Implementations using the Identified Dynamic Model

All implementations which utilize the identified dynamic model run at 100 Hz, matching the default ROS publishing rate of the dVRK software.

1) *Gravity Compensation:* For Gravity Compensation, we assume that the joint velocities $\dot{\mathbf{q}}^c$ and accelerations $\ddot{\mathbf{q}}^c$ are zero. Then, we substitute the estimated parameter $\hat{\boldsymbol{\theta}}$, Eq. 2 and Eq. 3 into Eq. 13 to obtain:

$$\boldsymbol{\tau}_g = G(\mathbf{q}^d) \quad (26)$$

Then, we substitute the real-time joint value measurements \mathbf{q}_{meas}^d from the dVRK software into Eq. 26 to compute the real-time gravity force $\boldsymbol{\tau}_g$ in joint space. The resulting torque command is sent to the physical dVRK via ROS, using the CRTC convention [37], to enable real-time gravity compensation in free space. This scheme is implemented open loop and the built-in PID controller is disabled during gravity compensation testing.

2) *Computed-Torque Feedforward:* Compared to the gravity compensation implementation, computed-torque feedforward accounts for joint dynamic movements, and thus the joint velocities and accelerations are no longer assumed to be zero. Then, substituting the estimated parameter $\hat{\boldsymbol{\theta}}$, Eq. 2 and Eq. 3 into Eq. 13 yields:

$$\hat{\boldsymbol{\tau}}_c = M(\mathbf{q}^d) \ddot{\mathbf{q}}^d + C(\mathbf{q}^d, \dot{\mathbf{q}}^d) + G(\mathbf{q}^d) \quad (27)$$

where $\hat{\boldsymbol{\tau}}_c$ is also known as the computed torques of the robot.

Then the computed torques can be smoothly integrated into the dVRK controller as a feedforward term, $\boldsymbol{\tau}_{ff}$:

$$\begin{aligned} \boldsymbol{\tau}_o &= \mathbf{K}_p(\mathbf{q}_{meas}^d - \mathbf{q}_{des}^d) + \mathbf{K}_d(\dot{\mathbf{q}}_{meas}^d - \dot{\mathbf{q}}_{des}^d) + \boldsymbol{\tau}_{ff} \\ \boldsymbol{\tau}_{ff} &= M(\mathbf{q}_{meas}^d) \ddot{\mathbf{q}}_{des}^d + C(\mathbf{q}_{meas}^d, \dot{\mathbf{q}}_{meas}^d) + G(\mathbf{q}_{meas}^d) \end{aligned} \quad (28)$$

where \mathbf{q}_{meas}^d and \mathbf{q}_{des}^d represent measured and desired joint values, the joint accelerations $\ddot{\mathbf{q}}_{des}^d$ are calculated by numerically differentiating the desired joint velocities, and $\boldsymbol{\tau}_o$ denotes the torque control output.

J. Simplified Variant for Gravity Compensation Implementation in dVRK Software

We additionally created a simplified statics-only variant of the gravity compensation model, suitable for easy integration into the dVRK's kilohertz frequency control loops. This model was developed by assuming $\dot{\mathbf{q}}^c = \ddot{\mathbf{q}}^c = 0$, and neglecting friction and spring effects, so that Eq. 1 simplifies to $\boldsymbol{\tau}_{rg} = G_{rg}(\mathbf{q}^d)$. We used the same barycentric dynamics parameters

as in Eq. 5, however in the static case we need only h_k and m_k . Finally, the last four joints and links are lightweight and friction-dominated, so our simplified model only retains the first three joints/links.

One of the benefits of simplifying the model so drastically is the significantly lower dimensionality of the state space. Rather than using excitation trajectories to collect data for parameter estimation, it is feasible to exhaustively explore the joint space of the first three joints and measure joint torques while holding the robot stationary at each position. We collected joint torque measurements at a total of 150 distinct positions, visiting each position multiple times from different directions to mitigate static friction hysteresis.

As in Eq. 13, this simplified model admits a linear formulation

$$\boldsymbol{\tau}_{rg}(\mathbf{q}^d) = \mathbf{Y}_{rg}(\mathbf{q}^d)\boldsymbol{\theta}_{rg} \quad (29)$$

where $\boldsymbol{\theta}_{rg}$ denotes the reduced statics parameters for simplified gravity compensation and \mathbf{Y}_{rg} denotes the corresponding reduced regressor.

Given N pairs of joint positions and observed motor torques $(\mathbf{q}_i^d, \boldsymbol{\tau}_i^m)$ where i denotes the i^{th} sample, we fit the model by minimizing the least-squares objective J_{rg} :

$$J_{rg}(\boldsymbol{\theta}_{rg}) = \frac{1}{2} \sum_{i=1}^N \|\mathbf{Y}_{rg}(\mathbf{q}_i^d)\boldsymbol{\theta}_{rg} - \boldsymbol{\tau}_i^m\|_2^2 \quad (30)$$

subject to similar physical consistency constraints as the full dynamics model: (1) link masses m_k must be positive, and (2) link centers of mass r_k are contained within the link's bounding box. We used BFGS-B [38] to perform this bound-constrained minimization.

For integration into the dVRK arm controller (which runs at 1-2 kHz depending on the configuration), we use the efficient recursive Newton-Euler algorithm, implemented in the open-source *cisst* libraries [39]. For every controller step, our gravity compensation model is evaluated, and the predicted joint torques are added as a feed-forward to the joint-level controller. Notably, this simplified approach can handle different PSM mounting angles without additional tuning via modifying the mounting angle dVRK configuration setting.

This implementation of simplified gravity compensation has been available to the community in the dVRK software stack since February 2025.

IV. EXPERIMENT SETUP

In our work, all experiments are conducted on the dVRK-Si PSM setup shown in Fig. 5. The PSM is mounted at a zero-degree inclination relative to the table on an 80/20 aluminum frame and secured to the table using three clamps.

For tests involving sinusoidal motion, we generate the reference trajectory using Eq. 31.

$$\begin{aligned} q_1^d &= \alpha_{ori} \sin(\omega_{gen} t) \\ q_2^d &= \alpha_{ori} \sin(\omega_{gen} t) \\ q_3^d &= 0.12 + \alpha_{pos} \sin(\omega_{gen} t) \\ q_4^d &= q_5^d = q_6^d = q_7^d = 0 \end{aligned} \quad (31)$$



Fig. 5. Experimental setup: dVRK-Si PSM is mounted at a zero-degree inclination relative to the table.

where t denotes the runtime, $\alpha_{ori} = 20^\circ$ and $\alpha_{pos} = 0.05$ m denote the amplitudes for the revolute and prismatic joints, respectively; and the frequency coefficient is set to $\omega_{gen} = 0.005$ rad/s (0.5 rad per time step at a 100 Hz update rate)

V. RESULTS

This section presents the results of experiments to assess the accuracy (Section V-A) and computational cost (Section V-B) of the predicted torque from the dynamics model, its performance for static gravity compensation (Section V-C) and dynamic trajectory tracking (Section V-D), and to compare the two gravity compensation implementations (Section V-E).

A. Accuracy of Dynamics Model

We evaluate the prediction accuracy of the identified dynamics model by comparing the model-predicted joint efforts $\hat{\boldsymbol{\tau}}$ with the corresponding measured joint efforts. Fig. 6 shows a representative segment of an excitation trajectory, where the predicted joint torques/forces closely follow the measured joint torques/forces for the main load-bearing joints (joints 1-3). Quantitatively, we report the normalized root mean square error (NRMSE) computed over the full excitation trajectory, defined as:

$$\text{NRMSE}(\%) = 100 \times \frac{\sqrt{\frac{1}{N} \sum_{k=1}^N (\tau_k - \hat{\tau}_k)^2}}{\sqrt{\frac{1}{N} \sum_{k=1}^N \tau_k^2}} \quad (32)$$

where N denotes the number of points in the full excitation trajectory. The resulting NRMSE values are shown in Table II.

TABLE II
NRMSE RESULTS FOR ALL JOINTS

Joint Idx	1	2	3	4	5	6	7
NRMSE (%)	7.43	10.57	21.91	36.28	45.29	45.49	87.56

We can see that the first three joint torque/force predictions align closely with the measured values, while the remaining joints exhibit higher NRMSE due to their substantially smaller torque magnitudes and high sensitivity to torque estimation noise or unmodeled transmission/friction effects. Overall, these results indicate that the identified model captures the dominant PSM dynamics required for model-based compensation.

Measured vs Predicted Joint Torques/Forces

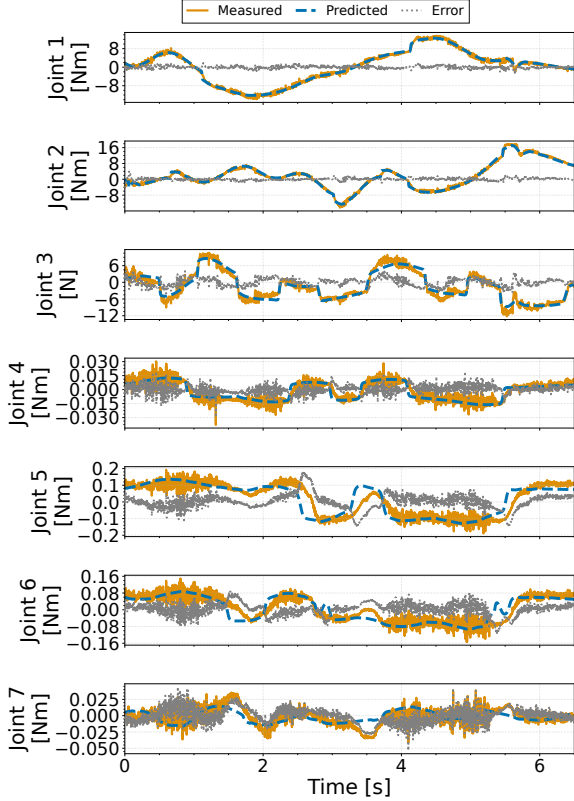


Fig. 6. Measured and model-predicted joint torques/forces over a representative segment of an excitation trajectory.

B. Runtime Performance of Dynamics Model

To evaluate the computational efficiency of the computed-torque term derived from the identified dynamic model, we measure the elapsed computation time for 10000 randomly generated joint configurations. The average computation time is 0.273 ms with a standard deviation of 0.004 ms on a AMD Ryzen™ 9 5950X CPU.

These results suggest that the inverse-dynamics evaluation using the identified model is computationally lightweight and can be performed within the time budget of low-level, real-time execution. In practice, the dominant bottleneck is the joint-state acquisition latency.

C. Gravity Compensation Evaluation (Static)

To validate our gravity compensation results, we perform a drift test by first moving the PSM to a desired pose using its position controller (a PD controller) and then switching to the (open-loop) gravity-compensation-torque-based control model described in section III-I1 for 5 seconds. The robot is considered to be drifting when moving more than 1 degree or 1 mm within the 5 seconds. We collect the kinematic data of the PSM and report the errors between the desired joint values and the measured joint values. We also determine the lower/upper bound torques (LB/UB τ) which, due to static friction, are sufficient to hold the joint in position. From Table I, we can see that gravity mainly influences the first three joints, and thus we only focus on those measurements and evaluations.

We select five random poses for testing and the results are shown in Table III.

TABLE III
DRIFT TEST RESULTS

Item	Pose Idx	PD	GC	PD	GC	Non-Drift	Non-Drift
		Pos Err	Pos Err	τ	τ	LB	UB
Joint1 (deg or N-m)	1	0.14	0.04	-1.42	-1.07	-0.11	-1.76
	2	0.06	0.04	0.60	1.25	0.43	2.17
	3	0.85	0.16	8.87	7.67	6.06	9.75
	4	0.50	0.11	-5.25	-6.39	-4.66	-7.99
	5	0.27	0.05	-2.81	-3.61	-2.48	-4.51
Joint2 (deg or N-m)	1	0.50	0.13	5.29	4.32	2.98	5.75
	2	0.45	0.12	4.67	5.73	3.84	7.34
	3	0.03	0.03	0.31	0.08	-0.87	0.85
	4	0.03	0.02	-0.32	-1.44	-0.18	-2.64
	5	0.37	0.14	-3.83	-2.97	-1.96	-4.61
Joint3 (mm or N)	1	1.49	0.25	-8.95	-7.79	-4.75	-9.35
	2	0.36	0.13	-2.19	-4.41	-2.07	-5.96
	3	0.46	0.63	-2.77	0.14	-2.79	2.03
	4	1.05	0.35	-6.31	-4.56	-1.83	-6.67
	5	0.78	0.39	4.68	2.97	0.92	4.78
Pose Idx		x	y	z	r_x	r_y	r_z
1		0.00	0.00	113.50	180.00	0.00	-90.00
2		-123.93	101.14	108.87	-126.83	-20.18	-65.27
3		-78.68	-50.46	-2.30	-88.59	-0.90	-122.65
4		50.10	-45.76	48.66	129.09	22.45	-64.83
5		174.45	67.87	-79.84	66.66	7.98	-79.84

Note for the table: The units of the poses are mm and deg. The 6D pose coordinates are based on the frame F_{RCM} shown in Fig. 4. GC stands for gravity compensation.

Results indicate that the gravity-compensation-torque-based control effectively maintains the robot's pose without noticeable drift. Furthermore, the gravity-compensation approach usually achieves a smaller steady-state error compared to the PD control. The joint torques generated by the gravity-compensation method for all three measured joints fall within their respective lower and upper bounds and, in most cases, are close to the midpoint of that range. For the third joint, some offset from the midpoint can be attributed to the significant friction in the prismatic joint and the cannula. Preliminary investigations also show that the gravity compensation can be generalized on different dVRK-Si PSMs with the same mounting-angle configuration.

D. Dynamic Tracking Accuracy Evaluation

We evaluate dynamic tracking performance by commanding the robot to track the sinusoidal reference trajectory in Eq. (31) under three conditions: (1) PID control only, (2) PID control with dVRK software gravity compensation (Section III-J), and (3) PID control with computed-torque feedforward (Section III-I2). The default dVRK-Si PID gains are used for all conditions. Results are shown in Fig. 7 and tracking error statistics are summarized in Table IV.

The results in Table IV show that the position tracking error is greatest in the PID only configuration, is somewhat reduced with gravity compensation (feedforward), and significantly reduced with the full computed-torque feedforward. Notably, this improvement is seen on all position tracking metrics (mean, STD, RMSE, and max), with the largest gains on the most gravity sensitive joint (the third joint).

The torque tracking error is similar between the three conditions, as expected since the PID feedback controller

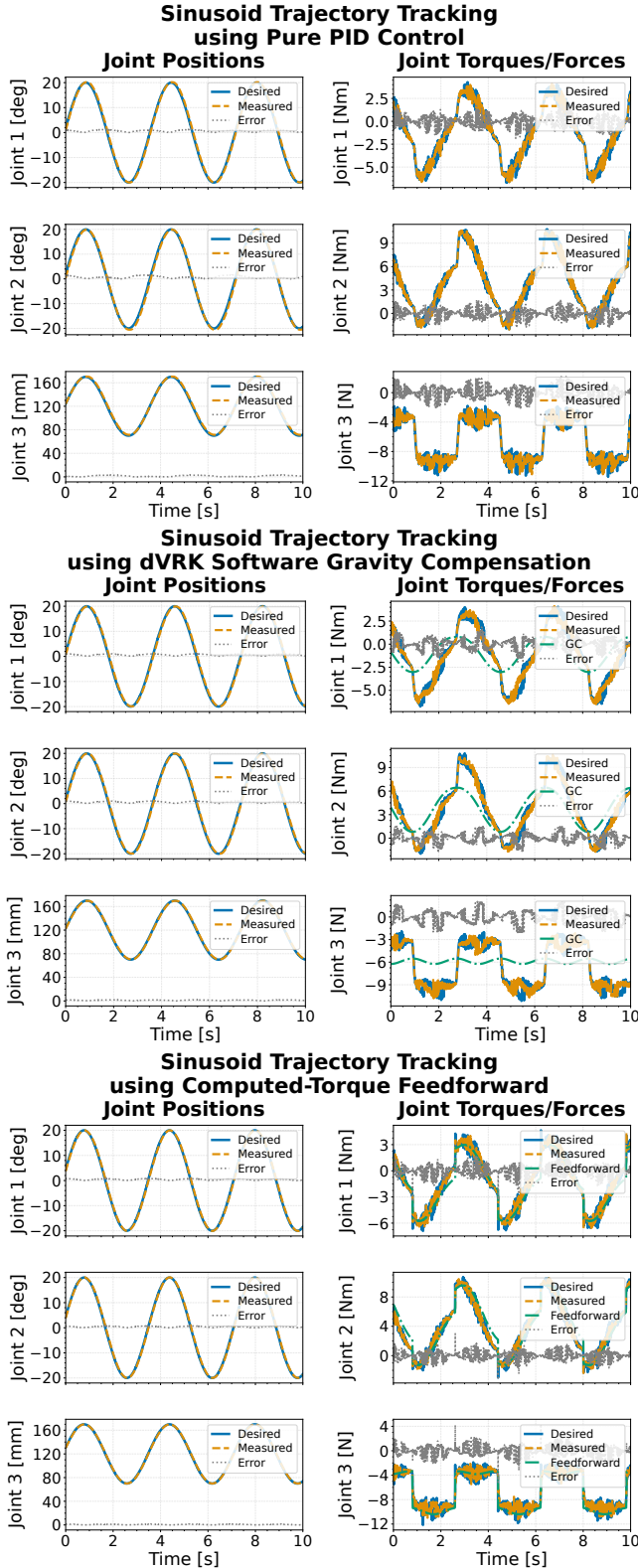


Fig. 7. Sinusoidal trajectory tracking using PID controller only (top), PID controller with dVRK software gravity compensation (middle), and PID controller with computed torque feedforward (bottom). Left panels compare desired and measured joint positions and report the position tracking error $\mathbf{q}_{err} = \mathbf{q}_{des} - \mathbf{q}_{meas}$. Right panels show the corresponding torque/force, including the desired joint efforts, measured joint efforts, and the errors between the measured and desired joint efforts $\boldsymbol{\tau}_{err} = \boldsymbol{\tau}_{des} - \boldsymbol{\tau}_{meas}$ over a 10 s trial.

TABLE IV
TRACKING ERROR STATISTICS

Item	Joint Idx	Mean	STD	RMSE	Max
Joint Position Errors (deg or mm)					
PID with Computed Torque Feedforward	1	0.46	0.24	0.52	0.94
	2	0.44	0.22	0.49	1.07
	3	0.78	0.40	0.88	1.57
PID with dVRK Software Gravity Compensation	1	0.68	0.30	0.74	1.13
	2	0.66	0.30	0.73	1.14
	3	1.25	0.46	1.33	2.05
PID only	1	0.70	0.35	0.78	1.27
	2	0.73	0.46	0.86	1.60
	3	1.35	1.02	1.70	3.11
Joint Torque Errors (Nm or N)					
PID with Computed Torque Feedforward	1	0.48	0.38	0.62	3.57
	2	0.48	0.37	0.61	3.05
	3	0.70	0.53	0.88	5.18
PID with dVRK Software Gravity Compensation	1	0.49	0.38	0.62	2.06
	2	0.49	0.38	0.61	2.10
	3	0.71	0.53	0.88	2.78
PID only	1	0.49	0.38	0.62	2.93
	2	0.49	0.38	0.61	2.42
	3	0.70	0.52	0.87	4.05

Note for the table: the joint position and torque errors are calculated by the difference between the desired (setpoint) and measured values acquired from the dVRK software, i.e. $\mathbf{q}_{err} = |\mathbf{q}_{des} - \mathbf{q}_{meas}|$ and $\boldsymbol{\tau}_{err} = |\boldsymbol{\tau}_{des} - \boldsymbol{\tau}_{meas}|$. **STD** and **RMSE** denote the standard deviation and root mean square error. Joints 1 and 2 are revolute joints and joint 3 is a prismatic joint.

compensates for the remaining torque required to attempt to follow the reference trajectory. This effect is illustrated in Fig. 8, which shows the torque output of the PID controller. In the case of the PID only configuration, this is the total torque applied to the motor, but in the other two conditions it is the residual torque that is added to the gravity or computed-torque feedforward terms. As seen in Fig. 8, the PID controller output with the computed-torque feedforward was much closer to zero than the other two configurations, indicating good accuracy of the dynamics model prediction. Interestingly, although most torque tracking metrics were similar, the maximum error was largest with the computed-torque feedforward. This may indicate that the computed-torque feedforward controller was more aggressive than the other two controllers, perhaps over-estimating the torque or exceeding actuator limitations.

E. Comparison of Gravity Compensation Methods

Figure 9 compares the two gravity compensation (GC) implementations while tracking the sinusoidal trajectory given by Eq. 31: (1) using the full dynamics model with velocity and acceleration set to zero (Section III-I1), and (2) the simplified gravity compensation model currently included in the dVRK software (Section III-J). In addition, the full computed-torque term is shown for reference. Both GC curves are smooth and periodic, which is consistent with a configuration-dependent gravity load, while the computed torque exhibits larger excursions and sharp transitions, reflecting additional motion-dependent dynamics (e.g., inertial/Coriolis terms) beyond gravity. The simplified gravity-compensation variant produces more conservative efforts because it ignores the friction and spring effects, reducing the risk of over-compensation.

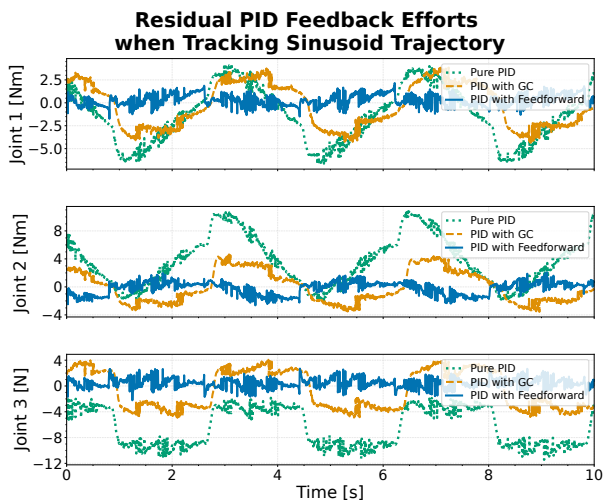


Fig. 8. Residual PID feedback joint torque/force comparison; contributions due to gravity compensation and computed-torque feedforward are excluded.

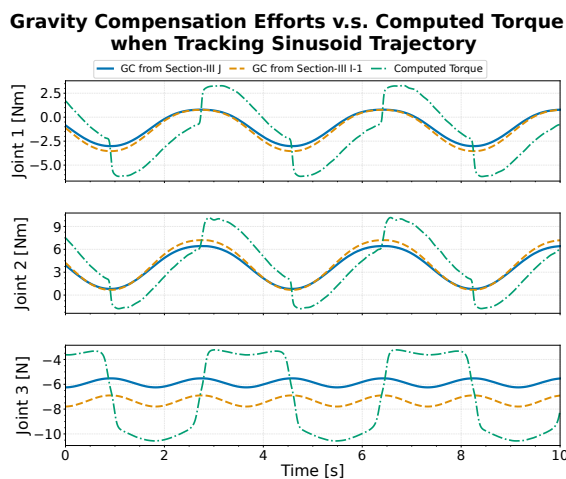


Fig. 9. Comparison of two gravity-compensation implementations (from Section III-I1 and Section III-J) and the full computed-torque term over a sinusoidal trajectory.

VI. DISCUSSION

The experimental results validate that the identified dynamics model is sufficiently accurate for model-based compensation on the dVRK-Si PSM. In particular, gravity compensation based on the identified model substantially improves static holding performance by reducing steady-state joint errors and end-effector drift, and it also reduces the feedback burden on the baseline PID loop during motion. Furthermore, incorporating the full inverse-dynamics term as a feedforward component can improve trajectory tracking accuracy beyond gravity-only compensation, indicating that the model captures motion-dependent dynamics that are not addressed by gravity compensation alone.

A practical implication of these findings is that different levels of model complexity are appropriate for different integration points in the dVRK control stack. The full dynamic model enables computed-torque feedforward and provides insight into torque limits and model prediction accuracy, while a simplified gravity-compensation variant can offer improved

robot robustness for high-rate execution.

A. Limitations

All experiments in this manuscript are conducted on a single dVRK-Si PSM mounted at a fixed inclination (zero-degrees) relative to the table, as shown in Fig. 5. Although preliminary observations suggest that the behavior of the gravity compensation approach in section III-I1 generalizes across different PSMs with the same mounting-angle configuration, a broader evaluation across multiple mounting angles, instruments, and hardware instances is still needed to fully characterize generalization and repeatability.

The computed-torque feedforward implementation runs at the default dVRK-ROS software update rate (100 Hz) and is currently limited by communication latency and the Python-based execution pipeline. These constraints can hinder low-level, real-time control at servo rates (e.g., full computed-torque control [40]).

B. Future Work

The current framework is implemented primarily in Python, but some existing C++ toolkits, such as the Pinocchio package [41], could be leveraged to accelerate inverse-dynamics computation and enable lower-latency, higher-rate execution.

Moreover, the PID gains used for sinusoidal trajectory tracking are kept identical across all control scenarios and are not re-tuned. As shown in Fig. 9, both gravity compensation and computed-torque feedforward reduce the residual PID feedback joint torques/forces. These results suggest that the PID gains should be fine-tuned for each scenario to achieve optimal tracking performance.

Last but not least, the higher NRMSE prediction errors on low-torque joints could motivate enhanced modeling of friction, hysteresis, and transmission effects (e.g., joint-specific friction regimes, backlash, cable-driven transmission nonlinearities, and cannula/trocar interactions). Incorporating these effects (or identifying them separately) is expected to improve both inverse-dynamics prediction accuracy and the reliability of model-based compensation during slow motions and direction reversals.

VII. CONCLUSION

This manuscript presented a complete modeling and identification framework tailored to the dVRK-Si PSM, including:

- 1) a kinematic formulation that accounts for the closed-chain parallelogram mechanism;
- 2) an Euler-Lagrange dynamics derivation expressed in linear-in-parameters form;
- 3) a physically consistent identification pipeline driven by an optimized excitation trajectory.

Using the identified parameters, we implemented real-time gravity compensation and computed-torque feedforward using the dVRK software package. Experiments on a physical dVRK-Si PSM demonstrated that model-based gravity compensation substantially improves static performance by reducing steady-state errors and end-effector drift, while computed-torque feedforward further improves trajectory tracking by compensating

motion-dependent dynamics beyond gravity. Overall, these results establish a practical foundation for reliable model-based control, realistic simulation, and downstream autonomy research on the dVRK-Si platform.

ACKNOWLEDGEMENT

Thanks to Dale Bergman, Alessandro Gozzi and the Intuitive Foundation for all the hardware support of the dVRK-Si.

REFERENCES

- [1] P. Kazanzides, Z. Chen, A. Deguet, G. S. Fischer, R. H. Taylor, and S. P. DiMaio, "An open-source research kit for the da Vinci® Surgical System," in *IEEE International Conference on Robotics and Automation (ICRA)*, 2014, pp. 6434–6439.
- [2] C. D’Ettorre, A. Mariani, A. Stilli, F. R. y Baena, P. Valdastri, A. Deguet, P. Kazanzides, R. H. Taylor, G. S. Fischer, S. P. DiMaio, A. Menciassi, and D. Stoyanov, "Accelerating surgical robotics research: A review of 10 years with the da Vinci Research Kit," *IEEE Robotics & Automation Magazine*, vol. 28, no. 4, pp. 56–78, 2021.
- [3] J. W. Kim, J.-T. Chen, P. Hansen, L. X. Shi, A. Goldenberg, S. Schmidgall, P. M. Scheikl, A. Deguet, B. M. White, D. R. Tsai *et al.*, "SRT-H: A hierarchical framework for autonomous surgery via language-conditioned imitation learning," *Science robotics*, vol. 10, no. 104, p. eadt5254, 2025.
- [4] K. Xu, J. Y. Wu, A. Deguet, and P. Kazanzides, "dVRK-Si: The next generation da Vinci Research Kit," in *International Symposium on Medical Robotics (ISMR)*. IEEE, 2025, pp. 185–191.
- [5] H. Yang, A. Acar, K. Xu, A. Deguet, P. Kazanzides, and J. Y. Wu, "An effectiveness study across baseline and learning-based force estimation methods on the da Vinci Research Kit Si system," *IEEE Transactions on Medical Robotics and Bionics*, vol. 7, no. 4, pp. 1393–1397, Nov. 2025.
- [6] H. Zhou, H. Yang, A. Deguet, L. Fichera, J. Y. Wu, and P. Kazanzides, "Gravity compensation of the dVRK-Si Patient Side Manipulator based on dynamic model identification," in *Hamlyn Symposium on Medical Robotics*, 2025, pp. 91–92.
- [7] G. A. Fontanelli, F. Ficuciello, L. Villani, and B. Siciliano, "Modelling and identification of the da Vinci Research Kit robotic arms," in *IEEE/RSJ International Conference on Intelligent Robots and Systems (IROS)*, 2017, pp. 1464–1469.
- [8] Y. Wang, R. Gondokaryono, A. Munawar, and G. S. Fischer, "A convex optimization-based dynamic model identification package for the da Vinci Research Kit," *IEEE Robotics and Automation Letters*, vol. 4, no. 4, pp. 3657–3664, 2019.
- [9] O. F. Argin, R. Moccia, C. Iacono, and F. Ficuciello, "daVinci Research Kit Patient Side Manipulator dynamic model using augmented Lagrangian particle swarm optimization," *IEEE Transactions on Medical Robotics and Bionics*, 2024.
- [10] H. Yang, H. Zhou, G. S. Fischer, and J. Y. Wu, "A hybrid model and learning-based force estimation framework for surgical robots," in *IEEE/RSJ International Conference on Intelligent Robots and Systems (IROS)*, 2024, pp. 906–912.
- [11] M. Ferro, A. Mirante, F. Ficuciello, and M. Vendittelli, "A CoppeliaSim dynamic simulator for the da Vinci Research Kit," *IEEE Robotics and Automation Letters*, vol. 8, no. 1, pp. 129–136, 2022.
- [12] H. Lin, C.-W. V. Hui, Y. Wang, A. Deguet, P. Kazanzides, and K. S. Au, "A reliable gravity compensation control strategy for dVRK robotic arms with nonlinear disturbance forces," *IEEE Robotics and Automation Letters*, vol. 4, no. 4, pp. 3892–3899, 2019.
- [13] H. Sang, J. Yun, R. Monfaredi, E. Wilson, H. Fooladi, and K. Cleary, "External force estimation and implementation in robotically assisted minimally invasive surgery," *The International Journal of Medical Robotics and Computer Assisted Surgery*, vol. 13, no. 2, p. e1824, 2017.
- [14] F. Piqué, M. N. Boushaki, M. Brancadoro, E. De Momi, and A. Menciassi, "Dynamic modeling of the da Vinci Research Kit arm for the estimation of interaction wrench," in *International Symposium on Medical Robotics (ISMR)*. IEEE, 2019, pp. 1–7.
- [15] N. Yilmaz, J. Y. Wu, P. Kazanzides, and U. Tumerdem, "Neural network based inverse dynamics identification and external force estimation on the da Vinci Research Kit," in *IEEE International Conference on Robotics and Automation (ICRA)*. IEEE, 2020, pp. 1387–1393.
- [16] J. Y. Wu, N. Yilmaz, U. Tumerdem, and P. Kazanzides, "Robot force estimation with learned intraoperative correction," in *International Symposium on Medical Robotics (ISMR)*. IEEE, 2021, pp. 1–7.
- [17] C. D. Sousa and R. Cortesao, "Physical feasibility of robot base inertial parameter identification: A linear matrix inequality approach," *The International Journal of Robotics Research*, vol. 33, no. 6, pp. 931–944, 2014.
- [18] G. Pilonetto, T. Chen, A. Chiuso, G. De Nicolao, and L. Ljung, *Regularized system identification: Learning dynamic models from data*. Springer Nature, 2022.
- [19] J. Zhang, N. Yilmaz, U. Tumerdem, and P. Kazanzides, "Learning based estimation of 7 DOF instrument and grasping forces on the da Vinci Research Kit," in *International Symposium on Medical Robotics (ISMR)*. IEEE, 2022, pp. 1–7.
- [20] N. Yilmaz, J. Zhang, P. Kazanzides, and U. Tumerdem, "Transfer of learned dynamics between different surgical robots and operative configurations," *International Journal of Computer Assisted Radiology and Surgery*, vol. 17, no. 5, pp. 903–910, 2022.
- [21] X. Chen, M. Kam, N. Yilmaz, A. Deguet, and A. Krieger, "Accuracy analysis and enhancement via transformer-based robot calibration of the da Vinci Research Kit Si (dVRK-Si)," *Journal of Medical Robotics Research*, p. 2550001, 2025.
- [22] B. Raucent, G. Campion, G. Bastin, J.-C. Samin, and P. Y. Willems, "Identification of the barycentric parameters of robot manipulators from external measurements," *Automatica*, vol. 28, no. 5, pp. 1011–1016, 1992.
- [23] L. Sciavicco and B. Siciliano, *Modelling and control of robot manipulators*. Springer Science & Business Media, 2012.
- [24] J. J. Murray and G. H. Lovell, "Dynamic modeling of closed-chain robotic manipulators and implications for trajectory control," *IEEE Transactions on Robotics and Automation*, vol. 5, no. 4, pp. 522–528, 1989.
- [25] P. Green, K. Worden, K. Atallah, and N. Sims, "The modelling of friction in a randomly excited energy harvester," in *International Conference on Noise and Vibration Engineering (ISMA)*, Leuven, Belgium, Sept. 2012.
- [26] P. Maes, J.-C. Samin, and P.-Y. Willems, "Linearity of multibody systems with respect to barycentric parameters: Dynamics and identification models obtained by symbolic generation," *Mechanics Based Design of Structures and Machines*, vol. 17, no. 2, pp. 219–237, 1989.
- [27] M. Gautier, "Numerical calculation of the base inertial parameters of robots," *Journal of Robotic Systems*, vol. 8, no. 4, pp. 485–506, 1991.
- [28] J. Swevers, C. Ganseman, D. B. Tukel, J. De Schutter, and H. Van Brussel, "Optimal robot excitation and identification," *IEEE Transactions on Robotics and Automation*, vol. 13, no. 5, pp. 730–740, 2002.
- [29] D. Ruiz, "A scaling algorithm to equilibrate both rows and columns norms in matrices," CM-P00040415, Tech. Rep., 2001.
- [30] X. Chen, R. S. Womersley, and J. J. Ye, "Minimizing the condition number of a Gram matrix," *SIAM Journal on Optimization*, vol. 21, no. 1, pp. 127–148, 2011.
- [31] R. E. Perez, P. W. Jansen, and J. R. Martins, "pyOpt: a Python-based object-oriented framework for nonlinear constrained optimization," *Structural and Multidisciplinary Optimization*, vol. 45, pp. 101–118, 2012.
- [32] D. Kraft, "A software package for sequential quadratic programming," *Forschungsbericht- Deutsche Forschungs- und Versuchsanstalt für Luft- und Raumfahrt*, 1988.
- [33] K. Yoshida and W. Khalil, "Verification of the positive definiteness of the inertial matrix of manipulators using base inertial parameters," *The International Journal of Robotics Research*, vol. 19, no. 5, pp. 498–510, 2000.
- [34] S. Traversaro, S. Brossette, A. Escande, and F. Nori, "Identification of fully physical consistent inertial parameters using optimization on manifolds," in *IEEE/RSJ International Conference on Intelligent Robots and Systems (IROS)*. IEEE, 2016, pp. 5446–5451.
- [35] S. Diamond and S. Boyd, "CVXPY: A Python-embedded modeling language for convex optimization," *The Journal of Machine Learning Research*, vol. 17, no. 1, pp. 2909–2913, 2016.
- [36] B. O’Donoghue, E. Chu, N. Parikh, and S. Boyd, "SCS: Splitting conic solver, version 2.0.2," <https://github.com/cvxgrp/scs>, 2017.
- [37] Y.-H. Su, A. Munawar, A. Deguet, A. Lewis, K. Lindgren, Y. Li, R. H. Taylor, G. S. Fischer, B. Hannaford, and P. Kazanzides, "Collaborative Robotics Toolkit (CRTK): Open software framework for surgical robotics research," in *Fourth IEEE International Conference on Robotic Computing (IRC)*. IEEE, 2020, pp. 48–55.
- [38] R. H. Byrd, P. Lu, J. Nocedal, and C. Zhu, "A limited memory algorithm for bound constrained optimization," *SIAM Journal on Scientific Computing*, vol. 16, no. 5, pp. 1190–1208, 1995.
- [39] A. Deguet, R. Kumar, R. Taylor, and P. Kazanzides, "The cisst libraries for computer assisted intervention systems," in *MICCAI Workshop on Systems and Arch. for Computer Assisted Interventions*, Midas Journal: <http://hdl.handle.net/10380/1465>, 2008.

- [40] B. Siciliano, O. Khatib, and T. Kröger, *Springer handbook of robotics*. Springer, 2008, vol. 200.
- [41] J. Carpentier, G. Saurel, G. Buondonno, J. Mirabel, F. Lamiroux, O. Stasse, and N. Mansard, “The Pinocchio C++ library: A fast and flexible implementation of rigid body dynamics algorithms and their analytical derivatives,” in *IEEE/SICE International Symposium on System Integration (SII)*. IEEE, 2019, pp. 614–619.